

Injection Molding of Semicrystalline Polymers.

II. Modeling and Experiments

A. I. ISAYEV,* T. W. CHAN, M. GMEREK, and K. SHIMOJO

Institute of Polymer Engineering, University of Akron, Akron, Ohio 44325-0301

SYNOPSIS

The injection molding of an isotactic polypropylene was computer-simulated with both quiescent and shear-induced crystallization taken into account. A one-dimensional finite difference model was used to simulate the filling, packing, and cooling stages of the injection-molding cycle. The Spencer-Gilmore equation was used to relate the density variations to the pressure and temperature traces in the packing simulation. The quiescent crystallization kinetics was modeled by the differential form of the Nakamura equation. The theory developed by Janeschitz-Kriegl and co-workers was used to model the shear-induced crystallization kinetics. The pressure traces during the filling and packing stages of the molding cycle, the thickness of the shear-induced crystallization layer, and the crystallinity profile throughout the thickness of the part were measured and compared with predicted values.

© 1995 John Wiley & Sons, Inc.

INTRODUCTION

The injection molding of thermoplastics is classified as one of the most important polymer-fabrication processes. The advantages of this process include a high output rate along with the ability to keep tight prescribed tolerances. The molding conditions and mold geometry have a great effect on the final part quality. As a result, it is desirable to develop computer codes based on the laws of nature to simulate this process. An accurate simulation can cut down on expensive tooling costs and predict the final physical properties of the molded part.

In the injection-molding process, the high flow rates used bring about considerable shear stresses in the molten polymer. For semicrystalline polymers, these stresses tend to effect a one-dimensional crystal growth near the mold wall, resulting in the shear-induced crystallization or skin layer of the part. The polymer in the core region of the part does not incur high enough stresses and is allowed to crystallize three-dimensionally in a process known as quiescent (or thermally induced) crystallization. Simulations

of the injection molding of semicrystalline polymers are very limited. Kamal and Lafleur¹ proposed a model to combine heat transfer with crystallization in injection molding. The temperature and crystallinity profiles were determined from crystallization parameters derived from experiments. More recently, they proposed^{2,3} a structure-oriented model of viscoelastic semicrystalline polymers. The non-isothermal crystallization kinetics was described by the generalization of the Avrami⁴ equation by Nakamura et al.⁵ Hieber and Chiang⁶ simulated the filling and packing stages of the injection molding of polypropylene (PP). They used a temperature-dependent specific heat of the polymer to account for the heat generated by the crystallization process. Crystallization effects on the density of the polymer were also taken into account, but the crystallization kinetics was not. Manzione⁷ developed an empirical equation describing the temperature dependence of the overall rate of crystallization. He was able to predict the crystallinity profile within an injection-molded part. All the above works and several others,⁸⁻¹¹ however, did not take into account the different crystal morphologies that develop in an injection-molded part. In other words, shear-induced crystallization was not considered because of the lack of existing models. Hsiung and Cakmak¹² performed a more realistic simulation of slow-crystal-

This article is dedicated to Professor Hermann Janeschitz-Kriegl on the occasion of his 70th birthday.

* To whom correspondence should be addressed.

lizing polymers in injection molding. The crystallization kinetics was described by the Nakamura equation,⁵ with the effects of shear on the crystallization process taken into account by making the parameters in the Nakamura equation stress-dependent. The dependence of these parameters on temperature and stress was expressed by empirical relationships. However, the material constants were estimated from literature data, some not even of the same material. They reported that the induction time decreases and the rate of crystallization increases with increasing shear stress. The predicted crystallinity profiles were in qualitative agreement with experiments. Most recently, these authors¹³ employed a Lagrangian approach in the simulation to obtain better agreement between the predicted and experimental crystallinity distributions in injection-molded parts. The effect of shear has also been considered by Haudin and Billon¹⁴ in simulating the filling stage of injection molding. They correctly predicted the thickness of the solidified layer during the filling stage. The empirical equation deduced by Monasse and Fryda¹⁵ was used to describe the crystallization kinetics, although it is not clear how the model parameters were determined.

The performance of injection-molded parts is strongly affected by the development of microstructure in the polymer. The morphology of injection-molded samples of PP has been studied by Kantz et al.,^{16,17} Fitchmun and Mencik,^{18,19} and Menges et al.,²⁰ among others. Their findings generally show a highly oriented skin layer along with spherulitic growth in the core region. The skin layer is responsible for such undesirable features as cleavability, warping, and stress whitening.²¹

The skin-layer thickness of injection-molded PP has been studied by various authors.²²⁻³¹ Most recently, Fujiyama and Wakino³¹ noted that the melt temperature used for injection molding has the greatest effect on the thickness of the skin layer. More specifically, as the melt temperature is decreased, the thickness of the skin layer increases. Also, they reported that the thickness of the skin layer decreases as the distance from the gate increases.

This is Part II of a study on the injection molding of semicrystalline polymers. Part I³² deals with material characterization. In Part II, here, a simulation of both the filling and packing stages of the molding cycle was carried out, with the incorporation of models for both quiescent and shear-induced crystallization. Among other things, the thickness of the shear-induced crystallization layer and the distribution of crystallinity in the molding will be pre-

dicted and compared with experimental results obtained under various molding conditions.

THEORY OF QUIESCENT CRYSTALLIZATION

For the kinetic description of quiescent crystallization occurring in the core region of the molding, we use the differential form of the Nakamura equation⁵:

$$\frac{d\xi}{dt} = nK(T)(1 - \xi)[- \ln(1 - \xi)]^{(n-1)/n} \quad (1)$$

where ξ is the degree of crystallinity; K , the rate constant; n , the Avrami index; T , the temperature; and t , the time. The Hoffman-Lauritzen expression³³ is adapted^{34,35} to describe the temperature dependence of the rate constant:

$$K(T) = (\ln 2)^{1/n} \left(\frac{1}{t_{1/2,0}} \right) \exp\left(- \frac{U^*/R}{T - T_\infty} \right) \times \exp\left(- \frac{K_g}{T\Delta T f} \right) \quad (2)$$

where $\Delta T = T_m^0 - T$ and $f = [(2T)/(T + T_m^0)]$. In the Hoffman-Lauritzen expression, R is the universal gas constant; T_m^0 , the equilibrium melting point; and f , a correction factor for the reduction in the latent heat of fusion as the temperature is decreased. Thus expressed, the kinetic model has four parameters other than n : $(1/t_{1/2,0})$ is a preexponential factor that includes all terms independent of temperature; U^* , the activation energy for segmental jump rate and may be given a universal value of 6284 J/mol; K_g , the nucleation exponent; and T_∞ may be taken as the glass-transition temperature minus 30 K.

The Nakamura equation makes no allowance for an induction period for nucleation. To determine the induction time for quiescent crystallization, the method of Sifleet, et al.³⁶ was used. The nonisothermal induction time can be obtained by a summation of isothermal induction times according to

$$\bar{t} = \int_0^{t_i} \frac{dt}{t_i(T)} = 1 \quad (3)$$

where \bar{t} is the induction time index; t_i , the isothermal induction time; and t_i , the nonisothermal induction time. For melt-crystallization, the isothermal in-

duction time is assumed to follow the Godovsky and Slonimsky³⁷ expression:

$$t_i = t_m(T_m^0 - T)^{-a} \quad (4)$$

where t_m and a are material constants independent of temperature. When considering a moving medium, eq. (3) is modified to the following form for the case of one-dimensional flow:

$$\frac{\partial \bar{t}}{\partial t} + u \frac{\partial \bar{t}}{\partial x} = \frac{1}{t_f(T)} \quad (5)$$

where u is the velocity component in the x -direction.

THEORY OF SHEAR-INDUCED CRYSTALLIZATION

A theory of shear-induced crystallization has been developed by Janeschitz-Kriegl and co-workers.^{21,38-41} In the earliest version, the so-called "model of utmost uniformity,"^{21,40} it is assumed that the crystals grow in three dimensions, though not necessarily to the same extent, and the growth rates and the nucleation rate have the same temperature dependence. It can be derived²¹ that

$$\begin{aligned} \frac{D\Psi_1}{Dt} &= \left(\frac{\dot{\gamma}}{\dot{\gamma}_a}\right)^2 \frac{1 - \Psi_1}{\tau} - \frac{\Psi_1}{\tau} \quad \text{where} \quad \frac{D\Psi_1}{Dt} \\ &= \frac{\partial \Psi_1}{\partial t} + u \frac{\partial \Psi_1}{\partial x} \end{aligned} \quad (6)$$

$$\Psi_1 = \frac{1}{\hat{g}(T)} \left(\frac{d\Psi_0}{dt} \right) \quad (7)$$

$$\Psi_0 = \left[\frac{\phi_0(t)}{2} \right]^{1/4} \quad (8)$$

and

$$\phi_0 = -\ln(1 - \xi) \quad (9)$$

where Ψ_1 is the probability for precursors of shear-induced crystallization to form, $\dot{\gamma}$, the shear rate; $\dot{\gamma}_a$, the critical shear rate of activation; and τ , the relaxation time for shear-induced crystallization; ξ , the degree of crystallinity; and \hat{g} , the geometric mean of the growth rates and the nucleation rate. The first term on the right-hand side of eq. (6) is the creation term. Once Ψ_1 reaches the value of unity, no further improvement of the aptitude for shear-induced crystallization can be achieved. The second

term describes the decay of Ψ_1 . The model parameters $\dot{\gamma}_a$, τ , and \hat{g} may be determined from a special kind of extrusion experiments as described in Part I.³² The parameters $\dot{\gamma}_a$ and τ are strong functions of the melt temperature. Here, they are both assumed to have an Arrhenius-type temperature dependence given by

$$\dot{\gamma}_a(T) = \dot{\gamma}_{a0} \exp\left(-\frac{E_a}{RT}\right) \quad (10)$$

and

$$\tau(T) = \tau_0 \exp\left(\frac{E_\tau}{RT}\right) \quad (11)$$

where $\dot{\gamma}_{a0}$, E_a , τ_0 , and E_τ are material constants independent of temperature. The parameter \hat{g} is given by

$$\hat{g}(T) = \frac{[-\ln(1 - \varepsilon)/2]^{1/4}}{At_i(T)} \quad (12)$$

where A is related to the ratio of the growth rates of quiescent and shear-induced crystallization; $t_i(T)$, the isothermal induction time for quiescent crystallization; and ε , the smallest measurable value of crystallinity that is observed when the induction time is reached. In Part I,³² it was found that for the PP studied parameter A approached unity as the temperature was lowered from 210 to 185°C, and its value was quite insensitive to changes in temperature. The quantity ε was taken as 0.01.

SIMULATION OF INJECTION MOLDING

Filling Stage

We consider here a one-dimensional cavity-filling process.^{42,43} To simulate this process, the transport equations must be solved. The governing equations for a one-dimensional strip flow are

$$\text{Continuity: } \frac{\partial}{\partial x}(b\bar{u}) = 0 \quad (13)$$

$$\text{Momentum: } \frac{\partial P}{\partial x} + \frac{\partial}{\partial y} \left(\eta \frac{\partial u}{\partial y} \right) = 0 \quad (14)$$

$$\text{Energy: } \rho C_p \left(\frac{\partial T}{\partial t} + u \frac{\partial T}{\partial x} \right) = K_{th} \frac{\partial^2 T}{\partial y^2} + \Phi + \dot{H} \quad (15)$$

where x is the axial direction; y , the gapwise direction; b , the half-gap thickness; \bar{u} , the average velocity across the half-gap thickness; P , the pressure; η , the viscosity; ρ , the density; C_p , the specific heat; K_{th} , the thermal conductivity; Φ , the viscous heating; and \dot{H} , the rate of heat generation by crystallization.

The average velocity \bar{u} across the half-gap thickness is given by

$$\bar{u} = \frac{1}{b} \int_0^b u \, dy \quad (16)$$

The viscosity function η may be given by the modified Cross model⁴⁴:

$$\eta(\dot{\gamma}) = \frac{\eta_0(T)}{1 + \left(\frac{\eta_0(T)\dot{\gamma}}{\tau^*}\right)^{1-m}} \quad (17)$$

where

$$\eta_0(T) = B \exp\left(\frac{T_b}{T}\right) \quad (18)$$

There are four model parameters: B , T_b , τ^* , and m . The effect of crystallization on the viscosity, if any, is assumed to be negligible. In general, the above assumption is not strictly satisfied, since the shear-induced or quiescent crystallization may lead to an increase of the melt viscosity as a function of degree crystallinity. However, many attempts made so far to evaluate this dependence at best can be described as qualitative in nature. Thus, more experimental work is required to elucidate the effect of crystallinity on the melt viscosity for a possible inclusion in simulation of the cavity filling in the injection molding.

The viscous heating term Φ in the energy equation is defined as

$$\Phi = \eta \dot{\gamma}^2 \quad (19)$$

The rate of heat generation by crystallization is

$$\dot{H} = \frac{D\xi}{Dt} H_\infty \quad (20)$$

where H_∞ is the total heat of crystallization and

$$\frac{D\xi}{Dt} = \frac{\partial \xi}{\partial t} + u \frac{\partial \xi}{\partial x} \quad (21)$$

The boundary conditions are

$$\begin{aligned} u &= 0 \quad \text{at} \quad y = b \\ \frac{\partial u}{\partial y} &= 0 \quad \text{at} \quad y = 0 \end{aligned} \quad (22)$$

The continuity and momentum equations may be combined into

$$\frac{\partial}{\partial x} \left(S \frac{\partial P}{\partial x} \right) = 0 \quad (23)$$

where S is the melt fluidity defined by

$$S = \int_0^b \frac{y^2}{\eta} \, dy \quad (24)$$

Packing Stage

In the simulation of the packing stage, we consider the local conservation of mass⁴²

$$\frac{\partial \rho}{\partial t} + \rho \frac{\partial u}{\partial x} = 0 \quad (25)$$

The density ρ is treated according to the equation of state given by Spencer and Gilmore⁴⁵:

$$(P + \hat{P}) \left(\frac{1}{\rho} - \frac{1}{\hat{\rho}} \right) = \hat{R}T \quad (26)$$

where \hat{P} , $\hat{\rho}$, and \hat{R} are material constants.

By integrating eq. (25) across the half-gap thickness, one obtains

$$\frac{\partial \bar{\rho}}{\partial t} + \frac{1}{b} \int_0^b \rho \frac{\partial u}{\partial x} \, dy = 0 \quad (27)$$

where $\bar{\rho}$ is the average density across the half-gap thickness. By treating ρ as a representative constant ρ_0 , eq. (27) can be written as

$$\frac{\partial \ln \bar{\rho}}{\partial t} = - \frac{1}{b} \frac{\partial}{\partial x} b \bar{u} \quad (28)$$

where

$$\bar{u} = - \frac{S}{b} \frac{\partial P}{\partial x} \quad (29)$$

Therefore, eq. (25) now has the form

$$\frac{\partial \ln \bar{\rho}}{\partial t} = \frac{1}{b} \frac{\partial}{\partial x} \left(S \frac{\partial P}{\partial x} \right) \quad (30)$$

By taking the derivative of eq. (26) with respect to P , one gets

$$(P + \bar{P}) \left(-\frac{\partial \rho}{\rho^2} \right) + dP \left(\frac{1}{\rho} - \frac{1}{\hat{\rho}} \right) = \hat{R}dT \quad (31)$$

This can be rewritten in the following form:

$$d \ln \rho = \frac{1 - \rho/\hat{\rho}}{P + \bar{P}} dP - \left(1 - \frac{\rho}{\hat{\rho}} \right) d \ln T \quad (32)$$

Equation (28) can now be written as

$$G(x, t) \frac{\partial P}{\partial t} - \frac{1}{b} \frac{\partial}{\partial x} \left(S \frac{\partial P}{\partial x} \right) = -F(x, t) \quad (33)$$

where

$$G(x, t) = \frac{1}{b} \frac{1}{(P + \bar{P})} \int_0^b \left(1 - \frac{\rho}{\hat{\rho}} \right) dy \quad (34)$$

and

$$F(x, t) = -\frac{1}{b} \int_0^b \left(1 - \frac{\rho}{\hat{\rho}} \right) \frac{\partial \ln T}{\partial t} dy \quad (35)$$

$F(x, t)$ and $G(x, t)$ can be used as the basis for a unified formulation for the postfilling stage of the injection-molding process.⁴² By using the assumption that the density is not a function of y , $G(x, t)$ reduces to

$$G(x, t) = \frac{1 - \rho/\hat{\rho}}{P + \bar{P}} \quad (36)$$

where ρ is equal to

$$\rho = \frac{\hat{\rho}(P + \bar{P})}{\hat{\rho}\hat{R}T + P + \bar{P}} \quad (37)$$

$F(x, t)$ can be solved by using Kramer's method:

$$F(x, t) = -\frac{1 - \rho/\hat{\rho}}{b} \int_0^b \frac{\partial \ln T}{\partial t} dy \quad (38)$$

Crystallization

In dealing with the crystallization kinetics, several assumptions were made: First, it was assumed that at each nodal point only one type of crystallization could occur, either quiescent or shear-induced. This assumption is justified based on the extrusion experiments through a slit die conducted in Ref. 32. The observations made there using an optical microscopy indicate the absence of spherulites in the layer near the wall where the shear-induced crystallization takes place. At the same time, spherulites are seen in the core region crystallized under quiescent conditions (see Fig. 7 in Ref. 32). To determine which type occurred, eqs. (5) and (6) were used. For numerical purposes, eq. (5) may be put into the following form:

$$\bar{t}_k = \frac{1}{t_l \left(\frac{1}{\Delta t} + \frac{u}{\Delta x} \right)} + \bar{t}_{k-1} \quad (39)$$

where the subscript "k" denotes the k-th time step, $\Delta t = t_k - t_{k-1}$, and $\Delta x = x_k - x_{k-1}$. Once \bar{t}_k reached unity (utilizing an absolute convergence criterion of 10^{-5}), quiescent crystallization was assumed to begin. The numerical integration of eq. (6) over the time increment Δt is given by the expression

$$\Psi_{1k} = \frac{\left(\frac{\gamma}{\gamma_a} \right)^2 \left(\frac{1 - \Psi_{1k-1}}{\tau} \right) - \frac{\Psi_{1k-1}}{\tau}}{\left(\frac{1}{\Delta t} + \frac{u}{\Delta x} \right)} + \Psi_{1k-1} \quad (40)$$

Using the initial condition that $\Psi_{10} = 0$ at $t = 0$, eq. (40) can be solved for each time step. Once Ψ_{1k} reached unity (using an absolute convergence criterion of 10^{-5}), shear-induced crystallization was assumed to take place. If the probability Ψ_1 for shear-induced crystallization reached unity before the induction time index \bar{t} for quiescent crystallization at a particular nodal point, then shear-induced crystallization would occur at that nodal point. Quiescent crystallization was assumed to occur at all nodal points except those at which shear-induced crystallization took place.

Once Ψ_{1k} reached unity, its value was assumed not to change, and the numerical forms of eqs. (7), (8), and (9) were used to calculate Ψ_{0k} , ϕ_{0k} , and ξ_k , respectively:

$$\Psi_{0k} = \Psi_{0k-1} + \Psi_{1k} \hat{g} \Delta t \quad (41)$$

Shear-induced Crystallization Characterization

Isothermal shearing experiments were conducted on a single-screw extruder (Killion KL-100) with a special slit die apparatus as described in Part I.³² Experiments were carried out at four different temperatures: 185, 190, 200, and 210°C.

Flow through the slit die was initiated and allowed to continue until steady-state conditions were met. At this point, the flow was stopped. The die was then quenched in water at ambient temperature. Quenching was performed at various rest times after the cessation of flow. Once the sample was cooled, it was taken out of the die.

To determine the skin-layer thickness and the relaxation time τ for shear-induced crystallization, the sample was cut using a diamond saw and a microtome as described in Part I.³² The skin layer was observed under a polarizing optical microscope. The birefringence was measured with the help of a compensator. The experimental details have been given in Part I.³²

Injection-molding Experiments

To verify the simulation results, injection-molding experiments were performed on a BOY-30M reciprocating screw injection-molding machine. The mold and delivery system dimensions are shown in Figure 1. Three flush-mounted pressure transducers were installed, one in the nozzle of the machine (position A) and two in the mold cavity (positions B and C), to trace the pressure buildup. A linear variable differential transducer (LVDT) was used to measure the screw displacement during the molding cycle. The signals from the LVDT and pressure transducers were fed to a data acquisition system consisting of an A/D converter and an IBM PC/AT computer along with a software DM-100 (Dataq Instruments, Inc.) and its accessories. The rate of data acquisition was 40 data points per second. The experiments were carried out at various molding conditions as listed in Table I.

Table I Injection-molding Conditions

Melt temperature (°C)	215, 230, 250
Mold temperature (°C)	15, 60
Injection speed (% maximum)	33, 66, 100
Packing time (s)	15, 30, 45
Holding pressure (bar)	60
Injection pressure (bar)	60
Plasticizing limit (mm)	35
Plasticizing speed (%)	30

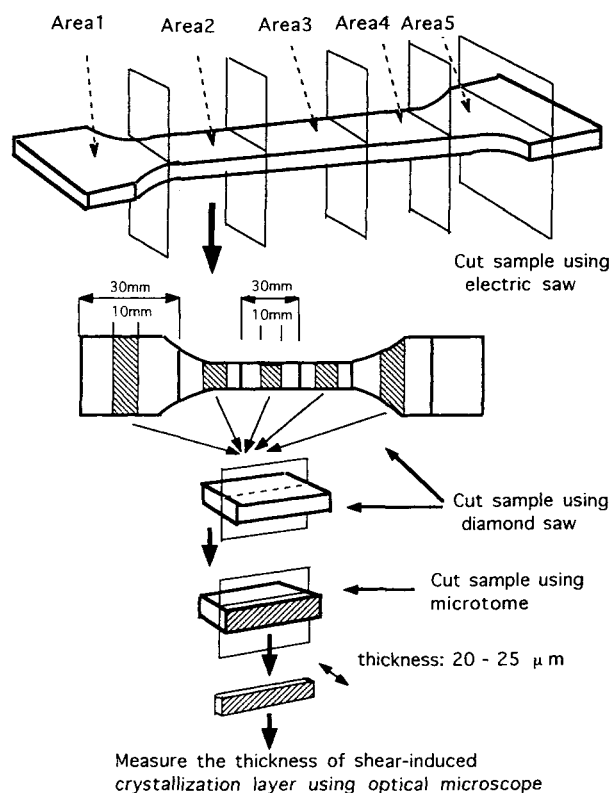


Figure 2 Sample cutting procedure in moldings for measurements of thickness of shear-induced crystallization layer.

Injection-molding experiments were also performed to show how the effect of freezing on the pressure transducers affects the pressure measurements. In these experiments, the mold temperature was increased in the following manner: 20, 60, 90, 120, 150, 180, and 230°C, until it reached the barrel temperature. Also, a small injection pressure was used (say 20 bar) so that no flashing would occur at the high mold temperatures.

Investigation of Injection-molded Samples

For morphology investigations, the injection-molded (dumbbell) samples were cut according to Figure 2, resulting in slices of about 20–25 microns thick in the width direction of the samples. These were set on glass slides and observed under a microscope to determine the thickness of the skin layer. Figure 3 gives optical photomicrographs of the sample indicating the various layers existing in the molding.

Starting from the surface of a sample cut from the central region of the molding, slices of approximately 30 microns were taken until 5 mg of the sample was obtained. This procedure was continued

in the gapwise direction until the center of the sample was reached. By then, six 5 mg samples were available for the determination of the distribution of crystallinity across the gap of the part. The degree of crystallinity was measured by the DSC in heating runs starting at 60°C and ending at 190°C. A scanning rate of 20°C/min was used in all the runs.

RESULTS AND DISCUSSION

Rheological Data

The modified Cross model [eqs. (17) and (18)] was fitted to the viscosity data obtained in Part I.³² The model parameter values $B = 2 \text{ g}/(\text{cm}\cdot\text{s})$, $T_b = 5066.5 \text{ K}$, $\tau^* = 1.2 \times 10^5 \text{ g}/(\text{cm}\cdot\text{s}^2)$, and $m = 0.34$ were found to fit the viscosity data well.

Physical and Thermal Properties

The thermal properties of the PP were assumed to remain constant throughout the simulations. Also, the density in the filling stage remained constant. The following values were taken from Chan et al.⁴⁶: thermal conductivity $K_{th} = 0.193 \text{ W}/(\text{m}\cdot\text{K})$, specific heat $C_p = 2.14 \text{ J}/(\text{g}\cdot\text{K})$, and density $\rho = 0.9 \text{ g}/\text{cm}^3$.

P-V-T Results

For a semicrystalline polymer like PP, a typical P-V-T curve consists of two linear regions with a transition zone in between. To cover the whole curve, two different fits were actually performed. The Spencer-Gilmore equation [eq. (26)] was used in the linear regions above and below the transition (crystallization) temperature. A fit of the transition region was taken from Hieber and Chiang⁶ that is represented by

$$\rho_t = 0 \quad \text{if } T > T_t$$

$$\rho_t = \frac{1}{b_7 \exp(b_8 \bar{T} - b_9 P)} \quad \text{if } T < T_t \quad (44)$$

where

$$T_t = b_5 + b_6 P \quad (45)$$

and

$$\bar{T} = T - b_5 \quad (46)$$

with the subscript t referring to the transition region. The material constants \hat{P} , $\hat{\rho}$, \hat{R} , b_5 , b_6 , b_7 , b_8 , and b_9

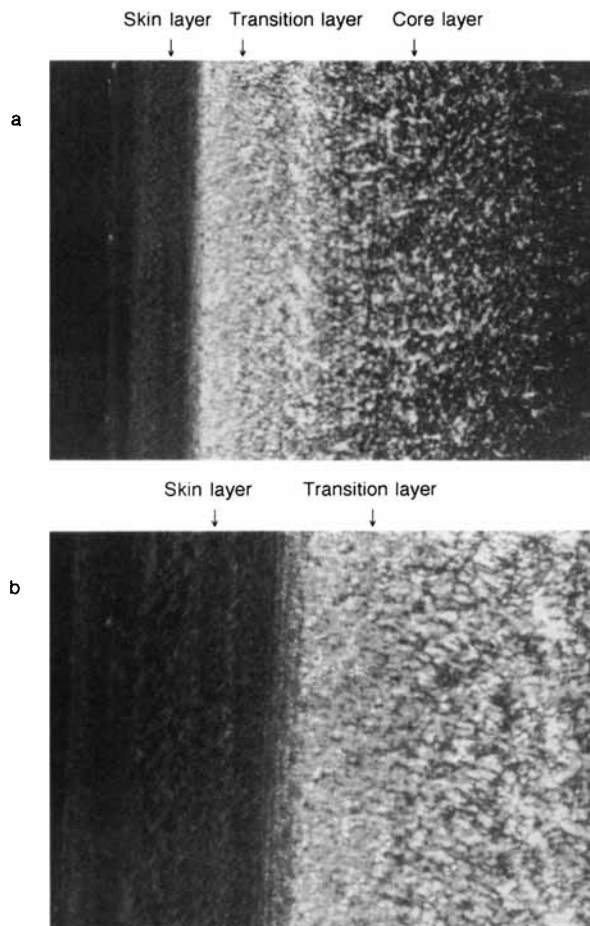


Figure 3 Optical photomicrographs of injection-molded sample indicating various layers: (a) $\times 40$; (b) $\times 100$.

are listed in Table II. A good fit was obtained for the P-V-T characterization, as can be seen in Figure 4.

Quiescent Crystallization Constants

The quiescent crystallization kinetic parameters were determined according to the method described in Part I.³² The values so obtained are $t_m = 8 \times 10^{11} \text{ s K}^6$, $a = 6$, $(1/t_{1/2})_0 = 2.07 \times 10^6 \text{ s}^{-1}$, and $K_g = 2.99 \times 10^5 \text{ K}^2$.

Shear-induced Crystallization Parameters

In Part I,³² the critical shear rate of activation $\dot{\gamma}_a$ and relaxation time τ were determined at four different temperatures. The best fit of eq. (10) to the experimental data of $\dot{\gamma}_a(T)$ gave $\dot{\gamma}_{a0} = 4.361 \times 10^{19} \text{ s}^{-1}$ and $E_a/R = 2.032 \times 10^4 \text{ K}$. The best fit of eq. (11) to the data of $\tau(T)$ yielded $\tau_0 = 1.735 \times 10^{-21} \text{ s}$ and $E_\tau/R = 2.5027 \times 10^4 \text{ K}$. The values of parameter

Table II Constants in Spencer–Gilmore Equation

If $T > T_i$:	$\hat{\rho} = 1.005 \frac{\text{g}}{\text{cm}^3}$	$\hat{P} = 2.402 \times 10^9 \frac{\text{dyne}}{\text{cm}^2}$
	$\hat{R} = 1.029 \times 10^6 \frac{\text{erg}}{\text{g K}}$	
If $T < T_i$:	$\hat{\rho} = 1.0837 \frac{\text{g}}{\text{cm}^3}$	$\hat{P} = 2.650 \times 10^9 \frac{\text{dyne}}{\text{cm}^2}$
	$\hat{R} = 2.203 \times 10^6 \frac{\text{erg}}{\text{g K}}$	$b_5 = 396 \text{ K}$
	$b_6 = 2.25 \times 10^{-7} \frac{\text{K}}{\text{Pa}}$	$b_7 = 8.7 \times 10^{-14} \frac{\text{cm}^3}{\text{g}}$
	$b_8 = 273.5 \text{ K}$	$b_9 = 1.26 \times 10^{-7} \text{ Pa}^{-1}$

A at four different temperatures are given in Table III.

Filling Stage of Injection Molding

Figures 5–8 show pressure vs. time for the filling stage and beginning of the packing stage under different molding conditions. The LVDT measurements of the screw displacement are also given in these figures. It can be seen that the predicted values of the pressure in the nozzle during the filling stage are lower than the measured values. This can be explained by the fact that pressure drops due to entrance effects in the runner system are neglected in the simulation. The agreement between the measured and simulated pressure values is good at the transducers located within the mold cavity. This is expected since no entrance effects take place within the cavity.

The LVDT readings during mold filling are almost linear with time. This confirms the validity of the constant flow rate assumption used in the simulation. Having an almost constant flow rate also contributes to the accuracy in the simulated pressure traces within the cavity.

From a comparison of pressure traces depicted in Figures 5 and 6, the effect of the melt temperature on the pressure during the filling stage can be observed. As expected, raising the melt temperature of the polymer lowers the pressure needed to push

the polymer into the mold. This can be attributed to a lower viscosity at higher melt temperature.

By comparing Figures 5 and 7, the effect of the flow rate on the pressure can be seen. The pressure needed to fill the mold increases with increasing flow rate, a result to be expected since the calculated pressure gradient is directly proportional to the flow rate.

Figures 6 and 8 show the effect of the mold temperature on the pressure at about the same flow rate. It takes a slightly higher pressure to fill the colder mold, a result consistent with a higher viscosity at lower mold temperature.

Packing Stage of Injection Molding

Figures 9–12 show pressure traces of the packing stage of the molding conditions used in Figures 5–

Table III Values of Parameter A

Temperature (°C)	A
185	0.9995
190	0.9992
200	0.998
210	0.993

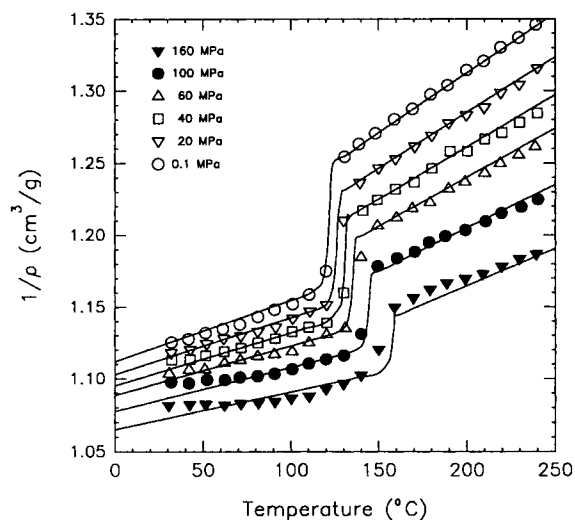


Figure 4 P–V–T curves for PP. Symbols represent experimental data taken from Hieber and Chiang⁶ and lines represent fit of Spencer–Gilmore equation to data.

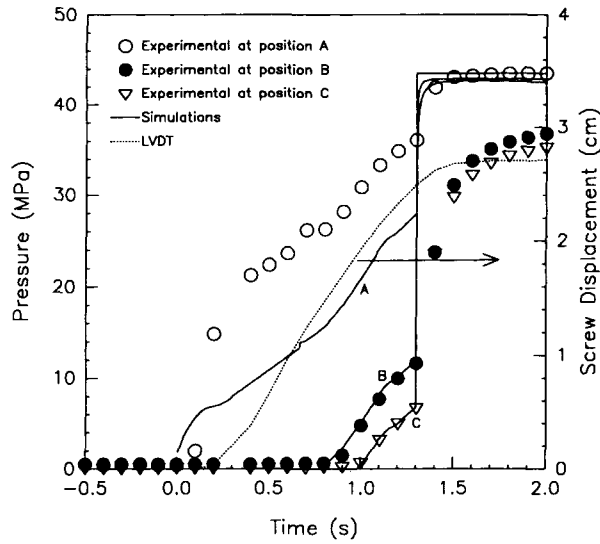


Figure 5 Pressure vs. time for 2 s of molding time. Molding conditions: $T_0 = 215^\circ\text{C}$, $T_w = 60^\circ\text{C}$, $Q = 13.2 \text{ cm}^3/\text{s}$. Positions A, B, and C correspond to pressure transducer locations in Figure 1.

8 over a period of about 45 s. Initially, the predicted pressures rise to the maximum faster than the experimental results indicate. The simulation employs an inelastic fluid model. Viscoelasticity of the polymer melt that is not taken into account in the simulation could explain this phenomenon. Also, the predicted pressure values within the cavity are much higher than the experimental values. During packing, it is expected that an almost uniform pressure field should develop after the filling stage is complete

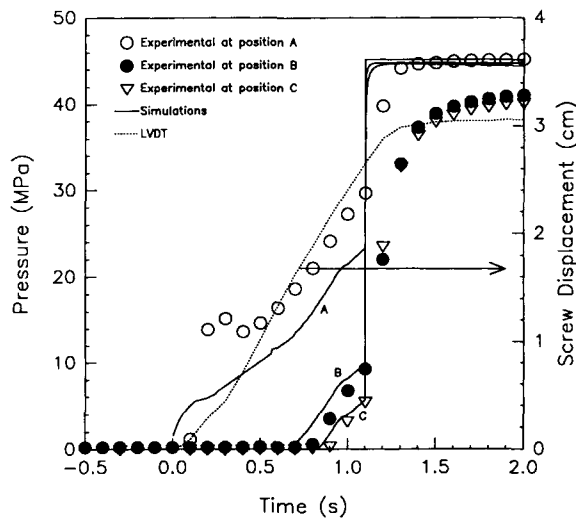


Figure 6 Pressure vs. time for 2 s of molding time. Molding conditions: $T_0 = 250^\circ\text{C}$, $T_w = 60^\circ\text{C}$, $Q = 15.6 \text{ cm}^3/\text{s}$.

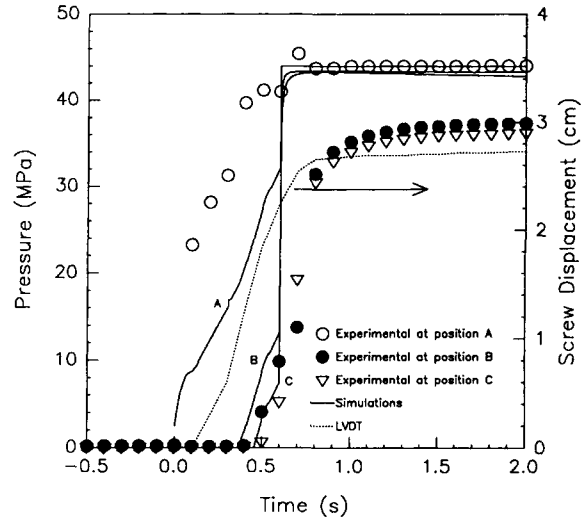


Figure 7 Pressure vs. time for 2 s of molding time. Molding conditions: $T_0 = 215^\circ\text{C}$, $T_w = 60^\circ\text{C}$, $Q = 28.6 \text{ cm}^3/\text{s}$.

and before the gate freezes. However, the experimental results do not show this behavior.

It was determined that the pressure difference between the nozzle and the pressure transducers in the cavity was due to melt-freezing effects on the transducers. Since the nozzle is kept at the melt temperature, no freezing effects are detected at this transducer. However, freezing effects do occur at the transducers located within the cavity of the cold mold. The effect of freezing was confirmed by molding experiments that were carried out by increasing the mold temperature until the melt temperature

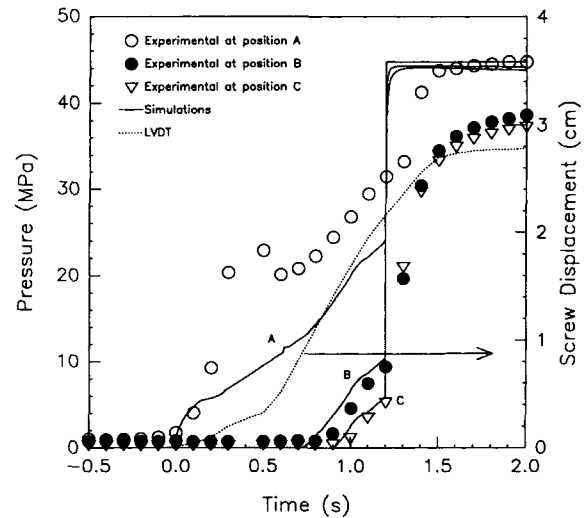


Figure 8 Pressure vs. time for 2 s of molding time. Molding conditions: $T_0 = 250^\circ\text{C}$, $T_w = 15^\circ\text{C}$, $Q = 14.3 \text{ cm}^3/\text{s}$.

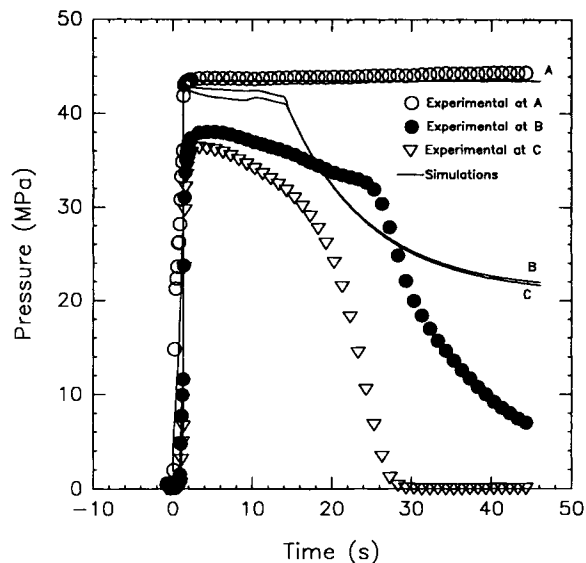


Figure 9 Pressure vs. time for complete molding cycle. Molding conditions: $T_0 = 215^\circ\text{C}$; $T_w = 60^\circ\text{C}$; $Q = 13.2 \text{ cm}^3/\text{s}$.

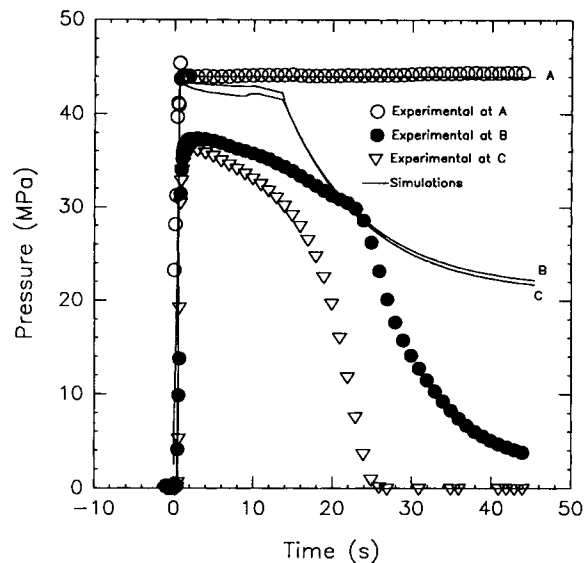


Figure 11 Pressure vs. time for complete molding cycle. Molding conditions: $T_0 = 215^\circ\text{C}$; $T_w = 60^\circ\text{C}$; $Q = 28.6 \text{ cm}^3/\text{s}$.

was reached. The pressure vs. time results of these experiments are shown in Figures 13 and 14. It can be seen that the pressure difference between the nozzle and the cavity decreases as the mold temperature is increased.

Referring back to Figures 9–12, other notable results are obtained. Just before the pressure starts to decay rapidly, a slight increase in pressure is observed. This is due to the sharp increase in density

near the crystallization temperature of the polymer. This phenomenon was also reported by Hieber and Chiang⁶ in modeling the injection molding of PP. When the temperature reaches the no-flow temperature of 103°C , the pressure starts to decay rapidly. This no-flow temperature for PP was determined from a DSC cooling run by Hieber and Chiang.⁶ The predicted pressure starts to decay before the experimental results. This may be caused by the mold

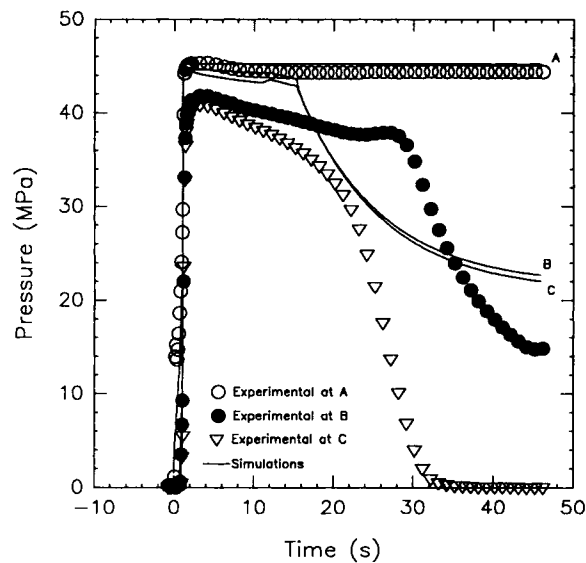


Figure 10 Pressure vs. time for complete molding cycle. Molding conditions: $T_0 = 250^\circ\text{C}$; $T_w = 60^\circ\text{C}$; $Q = 15.6 \text{ cm}^3/\text{s}$.

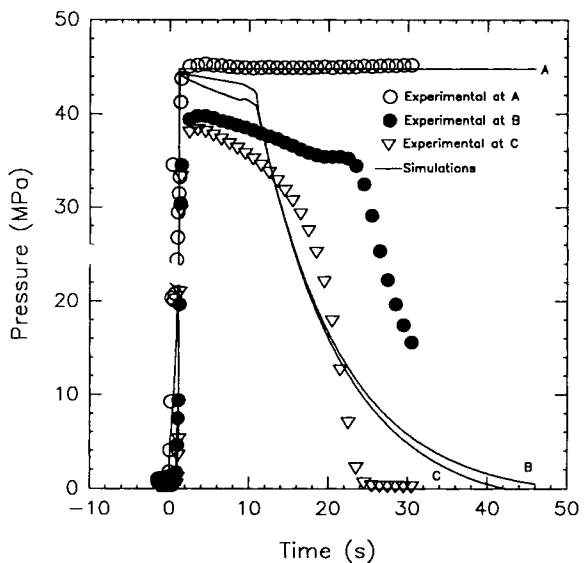


Figure 12 Pressure vs. time for complete molding cycle. Molding conditions: $T_0 = 250^\circ\text{C}$; $T_w = 15^\circ\text{C}$; $Q = 14.3 \text{ cm}^3/\text{s}$.

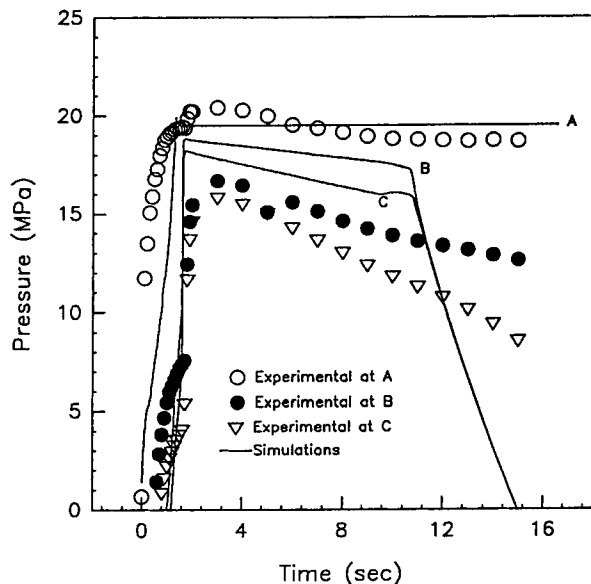


Figure 13 Pressure vs. time for complete molding cycle. Molding conditions: $T_0 = 250^\circ\text{C}$; $T_w = 20^\circ\text{C}$; $Q = 10.1 \text{ cm}^3/\text{s}$; injection pressure = 20 bar.

being at a temperature higher than the assumed constant mold temperature used in the simulations. This higher mold temperature is the result of viscous heating effects after many cycles of molding. Also, the simulated pressure at each transducer location within the cavity begins to decay at almost the same time. This can be explained as a limitation of the one-dimensional analysis used in the simulations.

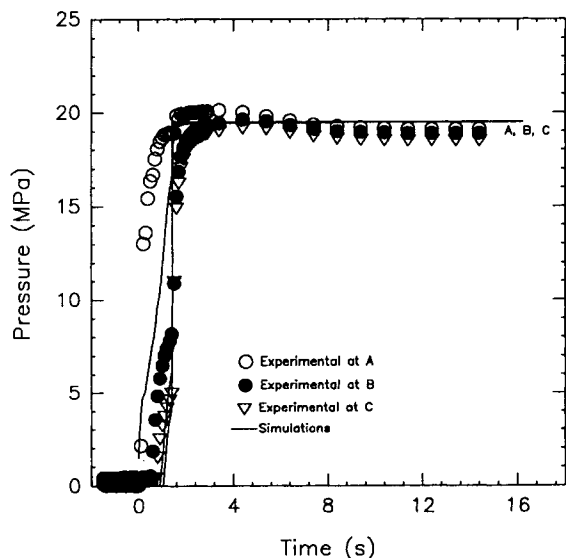


Figure 14 Pressure vs. time for complete molding cycle. Molding conditions: $T_0 = 250^\circ\text{C}$; $T_w = 230^\circ\text{C}$; $Q = 12.2 \text{ cm}^3/\text{s}$; injection pressure = 20 bar.

The pressure throughout the cavity would decay once the no-flow temperature is reached at one nodal point.

Simulation of Crystallization in Injection Molding

The microstructure of the injection-molded samples was studied. Specifically, the thickness of the skin layer was measured and compared with the simulated value. Figures 15–19 show the measured and predicted values of the normalized thickness of the skin layer as a function of distance from the gate. The normalized thickness is the thickness of the skin layer divided by the half-thickness of the sample.

In Figure 15, the effect of the melt temperature on the thickness of the skin layer is shown. It can be seen that the skin-layer thickness decreases with increasing melt temperature. This trend is shown by both the experimental and predicted results and can be explained by the critical shear rate of activation $\dot{\gamma}_a(T)$ and the relaxation time $\tau(T)$ functions [eqs. (10) and (11)]. As the temperature of the melt is increased, the polymer relaxes quicker and $\dot{\gamma}_a$ increases. The simulated results are in good agreement with the experimental measurements at the lowest melt temperature ($T_0 = 215^\circ\text{C}$). However, as the melt temperature increases, the difference between the predicted and experimental values increases. There are two explanations for this discrepancy:

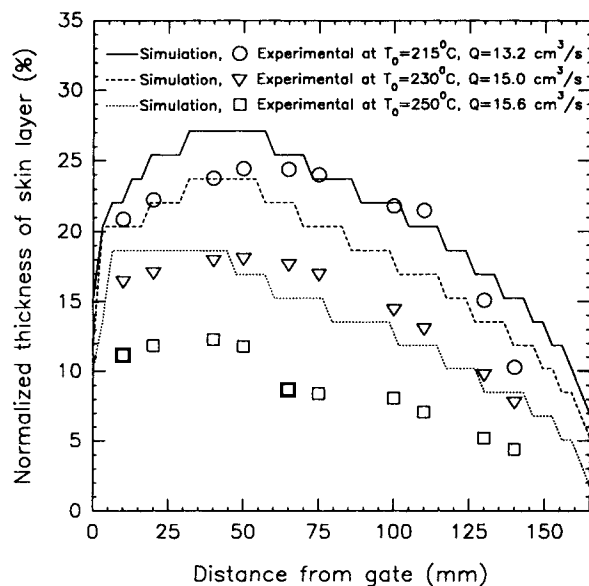


Figure 15 Normalized thickness of skin layer vs. distance from gate at different melt temperatures. Molding conditions: holding time = 45 s; $T_w = 60^\circ\text{C}$.

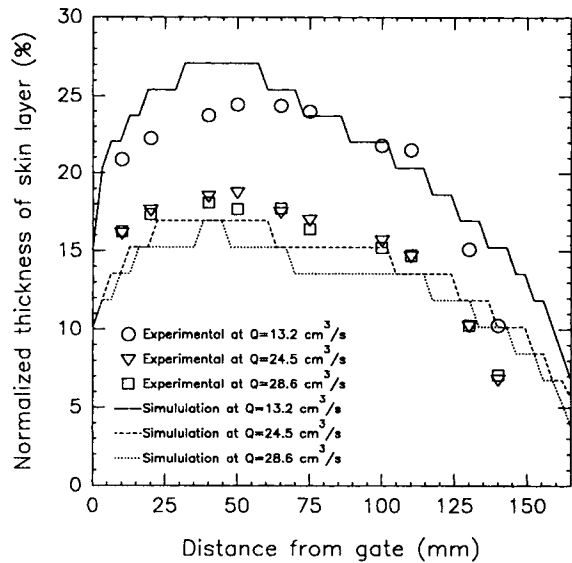


Figure 16 Normalized thickness of skin layer vs. distance from gate at different flow rates. Molding conditions: holding time = 45 s; $T_0 = 215^\circ\text{C}$; $T_w = 60^\circ\text{C}$.

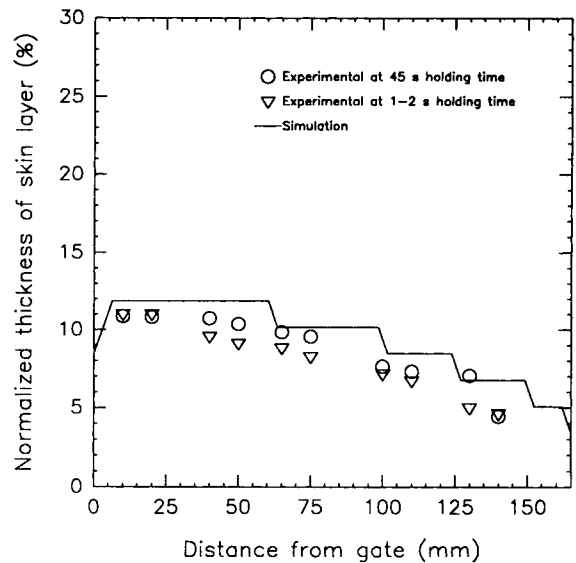


Figure 18 Normalized thickness of skin layer vs. distance from gate at two different holding times. Molding conditions: $T_0 = 215^\circ\text{C}$; $T_w = 15^\circ\text{C}$; $Q = 34.3 \text{ cm}^3/\text{s}$.

First, the isothermal shearing experiments used to determine the model parameters in Part I³² do not exactly coincide with the injection-molding process. In the shearing experiments, quenching was performed to freeze the shear-induced crystallization. The rest time was assumed to be the time between the cessation of flow and quenching. The temperature lag that exists between the quenching medium and the inner surface of the die was not taken into

account. In other words, the quench was not exact and the rest times were actually larger than the measured values. The effect becomes greater as the temperature of the melt is increased. This can explain the overprediction of the skin layer thickness as the melt temperature is increased. Another explanation for the overprediction is the assumed Arrhenius-type temperature dependence for the critical

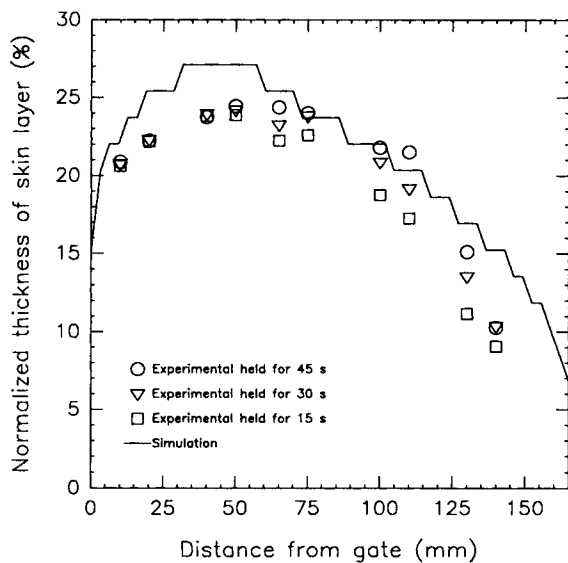


Figure 17 Normalized thickness of skin layer vs. distance from gate at three different holding times. Molding conditions: $T_0 = 215^\circ\text{C}$; $T_w = 60^\circ\text{C}$; $Q = 13.2 \text{ cm}^3/\text{s}$.

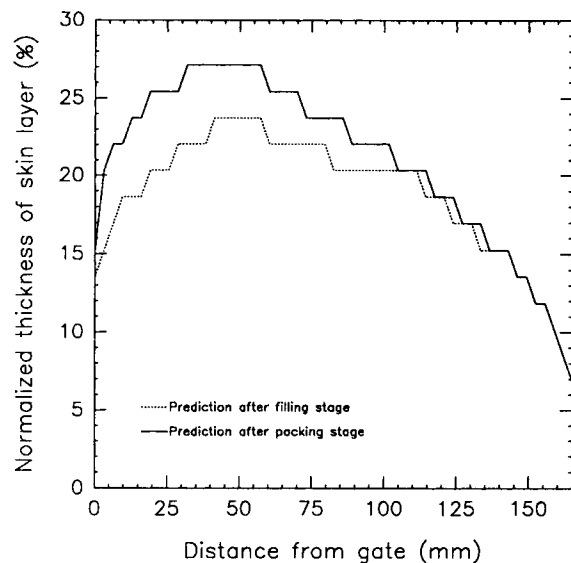


Figure 19 Predicted values of normalized thickness of skin layer vs. distance from gate after filling and after packing. Molding conditions: $T_0 = 215^\circ\text{C}$; $T_w = 60^\circ\text{C}$; $Q = 13.2 \text{ cm}^3/\text{s}$.

shear rate of activation $\dot{\gamma}_a$ and the relaxation time τ . Experimental values of $\dot{\gamma}_a$ and τ can be obtained only within a relatively narrow range of temperatures (between 185 and 210°C). Extrapolations of $\dot{\gamma}_a$ and τ to other temperatures could lead to large errors. More should be said about the effects of temperature on crystallization. First, isothermal conditions are difficult to realize because of the effects of viscous dissipation and heat of crystallization evolved. Often, a difference of 1 K could change the rate of crystallization by an order of magnitude. This point has been emphasized recently by Larsen and Hande.⁴⁷ Second, it was practically impossible to achieve an exact quench in the shearing experiments used to determine the model parameters as described in Part I³² and mentioned above, a difficulty previously acknowledged by Janeschitz-Kriegl and co-workers.²¹

Figure 16 shows the effect of the flow rate on the thickness of the skin layer. It can be concluded that the skin-layer thickness is larger at lower flow rates. It was first thought that the opposite effect would occur since higher flow rates mean higher shear rates within the mold. However, the shearing time seemed to be the dominant factor after further consideration. The lower flow rates allow the molten polymer to cool more near the mold wall during the filling stage. This, in turn, allows for more shear-induced crystallization to take place. It can be seen that the agreement between the measured and simulated values is good at all three flow rates considered. This good agreement is attributed to the fact that the melt temperature of 215°C used in these molding experiments is close to the melt temperature of 210°C in the extrusion experiments utilized to characterize shear-induced crystallization.

Figure 17 shows the thickness of the skin layer at three different packing pressure holding times (15, 30, and 45 s). It can be seen that the holding time variation does not have an effect on the thickness of the skin layer. The slight differences in the experimental measurements can be attributed to experimental errors. The predicted results agree quite well with the experimental results. From this figure, it can be concluded that the skin layer does not grow at least until after 15 s of holding time.

Figure 18 shows the skin-layer thickness at two different holding times under different molding conditions from those indicated in Figure 17. Again, the agreement between experimental and simulated results is quite good, and both show that there is no significant difference in the skin-layer thickness obtained between the two holding times. This means that shear-induced crystallization must be initiated

only in the filling stage and the brief packing stage (approximately 0.1 s) of the molding cycle. Unfortunately, it is impossible to experimentally measure the thickness of the skin layer just after filling is complete. However, predictions of this result can be obtained. Plots of the predicted skin-layer thickness at the end of the filling stage and after packing for 45 s are shown in Figure 19. These plots show that most of the shear-induced crystallization is initiated during the filling stage. The packing stage only contributes a small amount to the nucleation of shear-induced crystallization.

Figure 20 shows the effect of the mold temperature on the thickness of the skin layer. Both the experimental and predicted results show a slight increase in the thickness when the mold temperature is decreased. The colder mold provides greater cooling effects during filling, thus increasing the thickness of the skin layer.

Along with the thickness of the skin layer, the distribution of the degree of crystallinity throughout the thickness of the part was studied. The degree of crystallinity was determined from DSC heating runs using the following equation:

$$\xi = \frac{\Delta H_m - \Delta H_c}{\Delta H_f X_\infty} \quad (47)$$

where ΔH_m is the area under the melting peak; ΔH_c , the area under the crystallization peak; ΔH_f , the la-

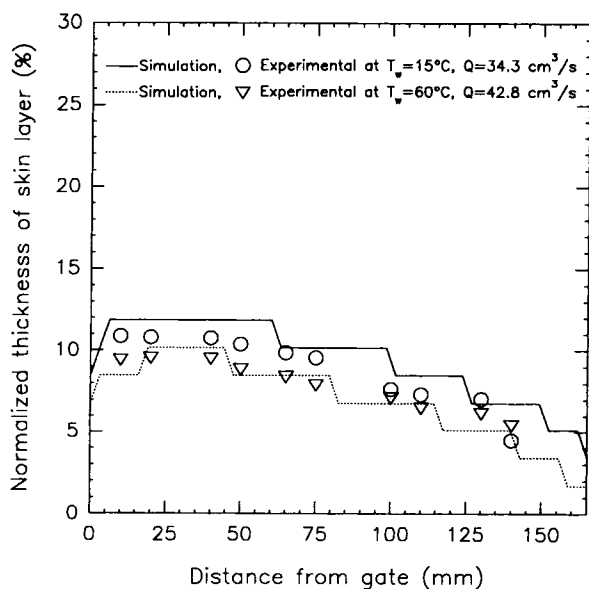


Figure 20 Normalized thickness of skin layer vs. distance from gate at two different mold temperatures. Molding conditions: Holding time = 45 s; $T_0 = 215^\circ\text{C}$.

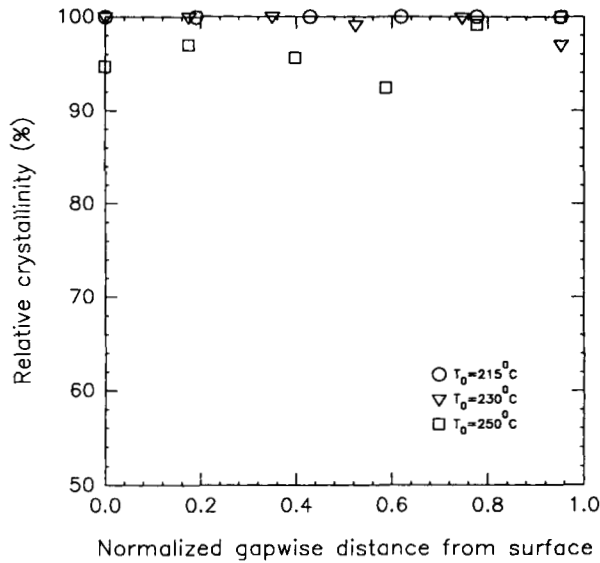


Figure 21 Crystallinity distribution throughout thickness of part at three different melt temperatures. Molding conditions: $T_w = 60^\circ\text{C}$; $Q = 13.2 \text{ cm}^3/\text{s}$.

tent heat of fusion of a perfect crystal ($= 2.09 \times 10^5 \text{ J/kg}$ for PP⁴⁸); and X_∞ , the ultimate degree of crystallinity ($= 0.4$ for PP⁴⁸).

Figure 21 shows the relative degree of crystallinity vs. the normalized gapwise distance from the surface of the part at three different melt temperatures. The experimental data show no crystallinity gradient and approximately 100% relative crystallinity throughout the thickness of the part, both results predicted by simulation. Another figure (Fig. 22) was devel-

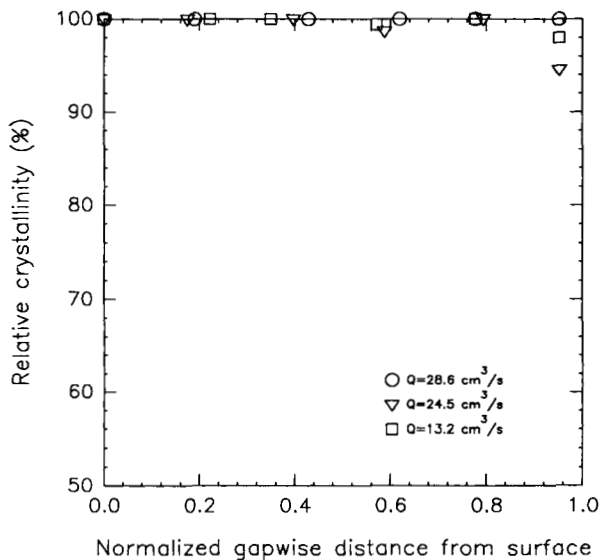


Figure 22 Effect of flow rate on crystallinity distribution. Molding conditions: $T_0 = 250^\circ\text{C}$; $T_w = 60^\circ\text{C}$.

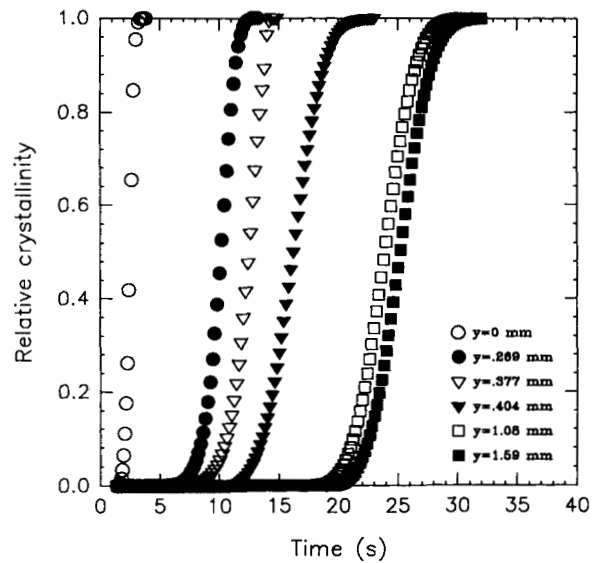


Figure 23 Predicted degree of crystallinity vs. time at six different locations throughout thickness of part. Molding conditions: $T_0 = 215^\circ\text{C}$; $T_w = 60^\circ\text{C}$; $Q = 13.2 \text{ cm}^3/\text{s}$.

oped to see if higher flow rates would effect a distribution of crystallinity. However, about 100% relative crystallinity was again obtained throughout the thickness of the part in each and every case.

Further studies were done on the modeling of crystallization in injection molding. The predicted degree of crystallinity vs. time was plotted in Figures 23 and 24 at two different melt temperatures. Six

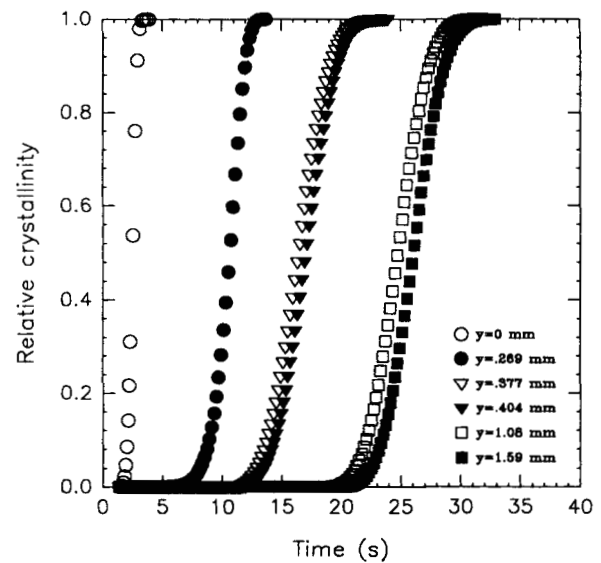


Figure 24 Predicted degree of crystallinity vs. time at six different locations throughout thickness of part. Molding conditions: $T_0 = 230^\circ\text{C}$; $T_w = 60^\circ\text{C}$; $Q = 13.2 \text{ cm}^3/\text{s}$.

different positions in the thickness direction midway in the length of the cavity were considered. In these plots, y denotes the distance from the surface of the part. The results are generally expected. The rate of crystallization is the greatest near the mold wall and gradually decreases as the center of the part is approached. However, it should be noted that at the boundary between shear-induced and quiescent crystallization the rate of crystallization decreases significantly when going from the shear-induced layer to the quiescent layer. This phenomenon can be seen in Figure 23 between the nodal points at $y = 0.377$ mm and $y = 0.404$ mm where the curves are substantially separated on the time scale. This increase in the overall rate of crystallization in the skin layer is probably due to an increase in the number of nuclei under shear flow.⁴⁹ Now, by observing Figure 24, this phenomenon does not occur between the same locations because quiescent crystallization takes place at both nodal points as a result of the higher melt temperature used.

The predicted degree of crystallinity vs. time at various distances from the gate was also plotted. This can be seen in Figure 25. Near the entrance of the mold the rate of crystallization is the greatest. However, the rate of crystallization seems almost uniform progressing into the cavity. The rate of crystallization was evaluated at the nodal point 1.08 mm from the surface of the part in the gapwise direction.

The predicted crystallinity profile in the gapwise direction as a function of time at the midway point

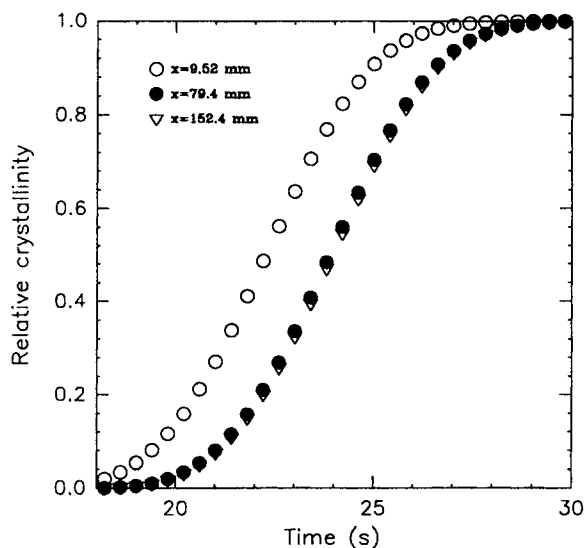


Figure 25 Predicted degree of crystallinity vs. time at three different locations throughout length of part. Molding conditions: $T_0 = 215^\circ\text{C}$; $T_w = 60^\circ\text{C}$; $Q = 13.2 \text{ cm}^3/\text{s}$.

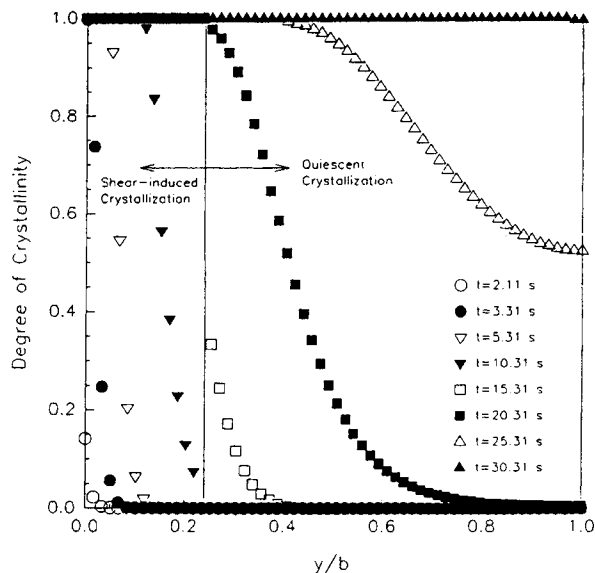


Figure 26 Predicted degree of crystallinity vs. normalized gapwise distance from surface of part as a function of time at midpoint of length of cavity. Molding conditions: $T_0 = 215^\circ\text{C}$; $T_w = 60^\circ\text{C}$; $Q = 13.2 \text{ cm}^3/\text{s}$.

in the length of the cavity is shown in Figure 26. The surface of the part is defined as $y = 0$. It is seen that the degree of crystallinity reaches unity much more rapidly near the surface of the mold than in the core region. The shear-induced crystallization (skin) layer can be easily distinguished from the core region crystallized in the quiescent state. At the boundary, there is a jump in crystallinity at $t = 15.31$ s.

The various predictions reported in this study must be considered quite good in view of the various experimental difficulties and simplifying assumptions involved. After all, this is just the first step toward the modeling of shear-induced crystallization in injection molding using the theory of Janeschitz-Kriegl et al. The tentative "model of uttermost uniformity," like the corresponding Nakamura equation used for quiescent crystallization, by its very nature precludes any prediction of the textures of the crystallized material. More realistic models capable of predicting textures have been proposed by Janeschitz-Kriegl et al.^{41,50,51} For the determination of model parameters, short-term shearing experiments have been performed. The process of nucleation is effectively separated from the subsequent crystal growth because during the short period of shear only primary nucleation has time to take place. The predicted distance between threadlike precursors are nicely corroborated by electron micrographs.⁴¹ However, the use of any of these models in the sim-

ulation of the injection molding of crystallizable polymers is still a task of the future.

CONCLUSIONS

The filling and packing stages of the injection molding of PP were studied. The study included experimental as well as simulated results of the pressure vs. time traces during both stages. Good agreement was obtained between the experimental and predicted results in the filling stage. However, there are discrepancies between the experimental and predicted values in the packing stage. This was attributed to the freezing effects on the pressure transducers that occurred in the experiments but were not accounted for in the simulations.

Both quiescent and shear-induced crystallization kinetics were taken into account in the simulations. The thickness of the shear-induced crystallization layer was experimentally measured and computer-simulated. Generally, the simulated results and the experimental data showed the same trend on the effect of processing conditions on the skin-layer thickness. The predicted results showed a good quantitative agreement with experiments conducted at low melt temperatures. The crystallinity profile across the thickness of the injection-molded sample was investigated. A uniform 100% relative crystallinity distribution was found both experimentally and numerically across the thickness of all samples. Finally, the rate of crystallization was studied numerically. Simulated results showed that the rate of shear-induced crystallization was substantially greater than that of quiescent crystallization. The rate was the greatest near the sample surface and decreased as the center of the sample was approached.

Financial support from the Ohio Board of Regents is gratefully acknowledged. The polypropylene used in this work was kindly supplied by Himont USA, Inc.

REFERENCES

1. M. R. Kamal and P. G. Lafleur, *Polym. Eng. Sci.*, **24**, 692 (1984).
2. P. G. Lafleur and M. R. Kamal, *Polym. Eng. Sci.*, **26**, 92 (1986).
3. M. R. Kamal and P. G. Lafleur, *Polym. Eng. Sci.*, **26**, 103 (1986).
4. M. Avrami, *J. Chem. Phys.*, **7**, 1103 (1939); **8**, 212 (1940); **9**, 117 (1941).
5. K. Nakamura, K. Katayama, and T. Amano, *J. Appl. Polym. Sci.*, **17**, 1031 (1973).
6. C. A. Hieber and H. H. Chiang, *Polym. Eng. Sci.*, **31**, 2 (1991).
7. L. T. Manzione, *SPE Tech. Pap.*, **33**, 285 (1987).
8. V. M. Nadkarni and J. P. Jog, *Plast. Eng.*, **August**, 37 (1984).
9. N. J. McCaffrey, C. Friedl, and R. Thomas, *SPE Tech. Pap.*, **36**, 382 (1990).
10. W. Y. Chiu, H. J. Tai, L. W. Chen, and L. H. Chu, *J. Appl. Polym. Sci.*, **43**, 521 (1991).
11. T.-Y. Chen, V. W. Wang, and M. J. Bozarth, *SPE Tech. Pap.*, **38**, 72 (1992).
12. C. M. Hsiung and M. Cakmak, *Polym. Eng. Sci.*, **31**, 1372 (1991).
13. C. M. Hsiung and M. Cakmak, in *Proceedings of the 10th PPS Annual Meeting*, Akron, 1994, p. 213.
14. J. M. Haudin and N. Billon, *Prog. Colloid Polym. Sci.*, **87**, 132 (1992).
15. B. Monasse and C. Fryda, in *Proceedings of the 6th PPS Annual Meeting*, Nice, 1990, p. 06-02.
16. M. R. Kantz, D. Newman, and F. H. Stigale, *J. Appl. Polym. Sci.*, **16**, 1249 (1972).
17. M. R. Kantz, *Int. J. Polym. Mater.*, **3**, 245 (1974).
18. D. R. Fitchmun and Z. Mencik, *J. Polym. Sci. Polym. Phys. Ed.*, **11**, 951 (1973).
19. Z. Mencik and D. R. Fitchmun, *J. Polym. Sci. Polym. Phys. Ed.*, **11**, 973 (1973).
20. G. Menges, G. Wubken, and B. Horn, *Colloid Polym. Sci.*, **254**, 267 (1976).
21. G. Eder, H. Janeschitz-Kriegl, and S. Liedauer, *Prog. Polym. Sci.*, **15**, 629 (1990).
22. A. Krosova, *Int. Polym. Sci. Technol.*, **4**, T/33 (1977).
23. H. Hirose, K. Ito, and T. Kawano, *Plast. Jpn.*, **26**(2), 13 (1980).
24. F. Altendorfer and G. Geymayer, *Plastverarbeiter*, **34**, 511 (1983).
25. F. Altendorfer and E. Seitzl, *Plastverarbeiter*, **35**, 144 (1984).
26. F. Altendorfer and E. Seitzl, *Kunststoffe*, **76**, 47 (1986).
27. J. Koppelman, E. Fleischmann, and G. Leiter, *Rheol. Acta*, **26**, 548 (1987).
28. G. Menges, H. Ries, and T. Wiegmann, *Kunststoffe*, **77**, 917 (1987).
29. E. Fleischmann and J. Koppelman, *Kunststoffe*, **78**, 453 (1988).
30. E. Fleischmann, *Int. Polym. Process.*, **4**, 158 (1989).
31. M. Fujiyama and T. Wakino, *J. Appl. Polym. Sci.*, **43**, 63 (1991).
32. A. I. Isayev, T. W. Chan, K. Shimojo, and M. Gmerek, **55**, 807 (1995).
33. J. D. Hoffman, G. T. Davis, and J. I. Lauritzen, in *Treatise on Solid State Chemistry: Crystalline and Non-Crystalline Solids*, J. B. Hannay, Ed., Plenum, New York, 1976, Vol. 3.
34. R. M. Patel and J. E. Spruiell, *Polym. Eng. Sci.*, **31**, 730 (1991).
35. T. W. Chan and A. I. Isayev, *Polym. Eng. Sci.*, **34**, 461 (1994).

36. W. L. Sifleet, N. Dinos, and J. R. Collier, *Polym. Eng. Sci.*, **13**, 10 (1973).
37. Yu. K. Godovsky and G. L. Slonimsky, *J. Polym. Sci. Poly. Phys. Ed.*, **12**, 1053 (1974).
38. G. Eder and H. Janeschitz-Kriegl, *Colloid Polym. Sci.*, **266**, 1087 (1988).
39. G. Eder, H. Janeschitz-Kriegl, and G. Krobath, *Prog. Colloid Polym. Sci.*, **80**, 1 (1989).
40. H. Janeschitz-Kriegl and G. Eder, *J. Macromol. Sci.-Chem. A*, **27**, 1733 (1990).
41. S. Liedauer, G. Eder, H. Janeschitz-Kriegl, P. Jerschow, W. Geymayer, and E. Ingolic, *Int. Polym. Process.*, **8**, 236 (1993).
42. C. A. Hieber, in *Injection and Compression Molding Fundamentals*, A. I. Isayev, Ed., Marcel Dekker, New York, 1987, Chap. 1.
43. M. Sobhanie and A. I. Isayev, in *Modeling of Polymer Processing*, A. I. Isayev, Ed., Hanser, Munich, 1991, Chap. 7.
44. M. M. Cross, *Rheol. Acta*, **18**, 909 (1979).
45. R. S. Spencer and G. D. Gilmore, *J. Appl. Phys.*, **20**, 502 (1949).
46. T. W. Chan, K. Shimojo, and A. I. Isayev, *SPE Tech. Pap.*, **39**, 1032 (1993).
47. A. Larsen and O. Hande, *Colloid Polym. Sci.*, **271**, 277 (1993).
48. C. H. Wu, G. Eder, and H. Janeschitz-Kriegl, *Colloid Polym. Sci.*, **271**, 1116 (1993).
49. M. D. Wolkowicz, *J. Polym. Sci. Polym. Symp.*, **63**, 365 (1978).
50. G. Eder, H. Janeschitz-Kriegl, and S. Liedauer, *Prog. Colloid Polym. Sci.*, **87**, 129 (1992).
51. S. Liedauer, G. Eder, and H. Janeschitz-Kriegl, to appear.

Received May 16, 1994

Accepted August 3, 1994